RESEARCH ARTICLE

PHYSICS

Optoelectronic tuning of plasmon resonances via optically modulated hot electrons

Jiacheng Yao[1], Cheng Wang[1], Chi Zhang[1], Song Ma[1], Li Zhou[1], Ti Wang[1], Ququan Wang[2], Hongxing Xu[1] and Tao Ding [ID][1],*

ABSTRACT

Fast optical modulation of nanoplasmonics is fundamental for on-chip integration of all-optical devices. Although various strategies have been proposed for dynamic modulation of surface plasmons, critical issues of device compatibility and extremely low efficiency in the visible spectrum hamper the application of optoplasmonic nanochips. Here we establish an optoplasmonic system based on Au@Cu$_{2-x}$S hybrid core–shell nanoparticles. The optical excitation of hot electrons and their charge transfer to the semiconductor coating (Cu$_{2-x}$S) lead to lowered electron density of Au, which results in the red shift of the localized surface plasmon resonance. The hot electrons can also transport through the Cu$_{2-x}$S layer to the metal substrate, which increases the conductance of the nanogap. As such, the coupled gap plasmon blue-shifts with a magnitude of up to ∼15 nm, depending on the excitation power and the thickness of the coatings, which agrees with numerical simulations. All of this optoelectronic tuning process is highly reversible, controllable and fast with a modulated laser beam, which is highly compatible and sufficiently useful for on-chip integration of nanophotonic devices.

Keywords: hot carriers, plasmon switching, optoplasmonics, circuit model, NPoM

[1] Key Laboratory of Artificial Micro/Nano Structure of Ministry of Education, School of Physics and Technology, Wuhan University, Wuhan 430072, China and [2] Department of Physics, Southern University of Science and Technology, Shenzhen 518055, China

*Corresponding author. E-mail: t.ding@whu.edu.cn

INTRODUCTION

Nanoplasmonic devices have been regarded as the fundamental component for the next generation of information technology due to its ultrafast speed, ultracompact size and extremely low heat dissipation [1]. Although this concept was brought in about a decade ago, the bottleneck issues of modulation speed and depth as well as compatibility with existing optoelectronic technology have not been satisfactorily resolved. For instance, although diverse plasmon switching strategies have been developed, most of them are slow in speed unless optical or optoelectronic means are applied [2]. Thus, optical modulation of surface plasmons based on the pump-probe technique has been developed but high pump power is required for an appreciable change [3–5]. Other optical switching strategies based on photothermal effect [6–10] or optoelectronic effect [11–14] are either not device-compatible or only suitable for the middle infrared (MIR) or near infrared (NIR) region, which does not align

well with the theme of optical communication and computation.

Direct modulation of the carrier density of the plasmonic components with light is possible but the efficiency is low unless a quantum tunneling region is reached [15]. It is critical that the conductance of the gap materials can be modulated by light in the order of dozens of G_0 (quantum conductance) [16], which is not applicable for most inorganic/organic materials [17]. Perhaps the ideal material for ultrafast plasmon switching is vanadium dioxide with Mott transition [18,19], which, however, is challenging to fit into plasmonic hotspots with a thickness of a few nanometers [20–22].

Cu$_{2-x}$S is a narrow-bandgap material that has shown strong capability of charge transfer (CT) for plasmon tuning [23]. However, this tuning strategy is slow and not reversible as it is based on wet chemistry, which makes it notoriously incompatible for device-based applications. Here we attempt to optically modulate the plasmon resonances of
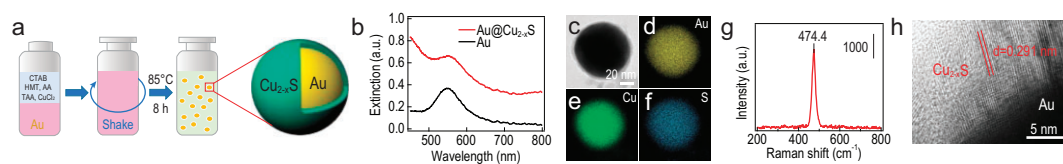
Figure 1. Synthesis of Au@Cu$_{2-x}$S core–shell NPs and their characterizations. (a) Synthetic procedure of Au@Cu$_{2-x}$S core–shell NPs. (b) Extinction spectra of Au and Au@Cu$_{2-x}$S core–shell NPs. (c) TEM and (d)–(f) elemental mapping of the Au@Cu$_{2-x}$ NPs. (g) Raman spectrum of Au@Cu$_{2-x}$S NPs. (h) HRTEM image of a typical Au@Cu$_{2-x}$S core–shell NP.

Au@Cu$_{2-x}$S core–shell nanoparticles (NPs), which show reversible red shift of localized surface plasmon resonance (LSPR) due to the deficiency in electron density on Au caused by the CT process. In contrast, when these Au@Cu$_{2-x}$S NPs are placed on Au films, conductance of the nanogaps is boosted by this CT, which results in reversible blue shift of the coupled plasmons. Both the experimental data and numerical analysis consistently support the proposed mechanism of optoelectronic tuning of surface plasmons, which is based on the optical attenuation of the plasmonic hot electrons. This type of tuning mechanism offers the possibility of fast plasmonic switching with light programmability and remote controllability, which are highly compatible for optoplasmonic devices.

RESULTS AND DISCUSSION

The Au@Cu$_{2-x}$S NPs were synthesized via sol–gel chemistry, where the Cu^{2+} ions are partially reduced by ascorbic acid (AA) and combine with S^{2-} ions disassociated from thioacetamide (TAA). As a result, the Cu$_{2-x}$S NPs grow on the Au NPs via heterogeneous nucleation, forming Au@Cu$_{2-x}$S core–shell NPs with variable shell thickness (Fig. 1a). The slight red shift ($\sim$5 nm) of extinction spectra suggests the coating of the Cu$_{2-x}$S shells due to the increase in the refractive index (RI) (Fig. 1b). Transmission electron microscope (TEM) imaging and energy dispersive X-ray spectroscopy (EDS) confirm that the shell has a thickness of $\sim$5 nm with elements of Cu and S (Fig. 1c–f). X-ray photoelectron spectroscopy (XPS) along with the Auger spectrum further confirms the presence of Cu(I) in the Au@Cu$_{2-x}$S NPs (Supplementary Figure S1) [24]. Raman spectrum of the Au@Cu$_{2-x}$S NPs presents a prominent peak at 474.4 cm^{-1}, which is attributed to the stretching of the S–S bond [25]. High-resolution TEM (HRTEM) further reveals the crystalline feature of the Cu$_{2-x}$S shells, which agrees with its lattice constant as reported in the literature [26]. The hybrid core–shell particles are normally dispersed in aqueous solution, which can be drop-casted on SiO$_2$/Si wafer (Fig. 2a)

or Au substrate (Fig. 2f) for light-induced plasmon switching.

For Au@Cu$_{2-x}$S NP on SiO$_2$/Si substrate, it shows weak electric (E)-field enhancement ($\sim$5) with LSPR (Fig. 2b). Illumination from a continuous wave (CW) laser (446 nm) on the Au@Cu$_{2-x}$S NP results in a $\sim$10-nm red shift of the scattering peak, which can switch back when the laser is turned off (Fig. 2c). This light-induced plasmon tuning is fully reversible for many cycles of light on and off (Fig. 2d and e), which excludes the possibility of irreversible particle deformation during the laser irradiation as shown previously [27]. On the contrary, the structure of Au@Cu$_{2-x}$S NP on Au film with strong E-field enhancement ($\sim$20, Fig. 2g) shows blue shift ($\sim$15 nm) of the scattering peak with laser illumination, which can shift back when the laser is switched off (Fig. 2h). Note that photoluminescence (PL) signals of plasmons are also collected during the laser excitation [28,29], which are subtracted to reflect the real change in white light scattering (Supplementary Figure S2). This blue shift, again, is fully reversible for many cycles of laser on and off (Fig. 2i and j).

This peculiar contrast suggests that some unique underlying mechanism is involved. As is well known, plasmon shift is normally induced by a change in RI, a change in separation and a change in charge density [2]. The former two are likely as the deformation of Cu$_{2-x}$S or the change in RI induced by the photothermal effect of laser irradiation can result in the shift of plasmon as revealed previously [30,31]. This is a reasonable assumption as the local temperature can reach $\leq$400°C for both 446- and 641-nm laser irradiation (Fig. 3a), which is sufficient to cause the phase change of Cu$_{2-x}$S [32]. However, we observe a slight blue shift ($\sim$3 nm) or no shift with 641-nm laser irradiation for Au@Cu$_{2-x}$S on SiO$_2$/Si or Au substrate (Supplementary Figure S3a and b), suggesting that these shifts of plasmon resonance are not likely caused by the increase in temperature. Moreover, for the observed 15-nm blue shift, it theoretically requires a decrease of 0.2 in RI or an increase of $\sim$8 nm in gap size (Fig. 3b and c and Supplementary Figure S4), which, however, is not likely as the RI of Cu$_{2-x}$S tends to increase
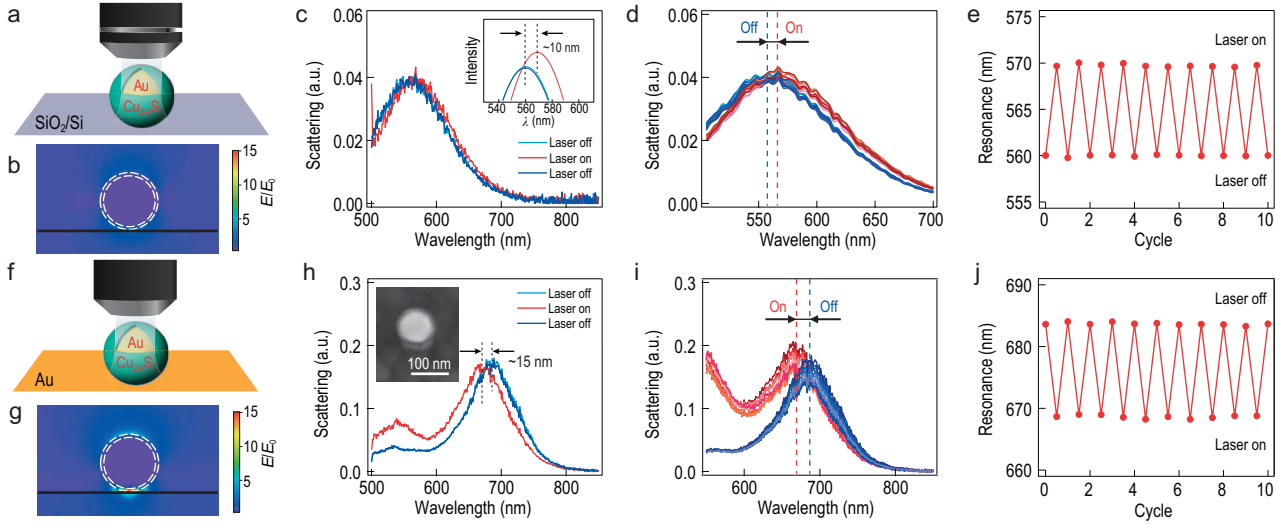
Figure 2. Laser-induced plasmon switching of Au@Cu$_{2-x}$S NPs on (a)–(e) SiO$_2$/Si substrate and (f)–(j) Au substrate. (a) and (f) Schematic of laser-induced switching; (b) and (g) electric near-field profile; (c) and (h) scattering spectra of Au@Cu$_{2-x}$S with laser switched on and off; (d) and (i) scattering spectra of Au@Cu$_{2-x}$S with cycles of laser on and off; and their (e) and (j) reversible resonance shifts with cycles of laser on and off.

and the thickness decreases due to the phase change [32,33]. Therefore, the only possibility it seems is the change in carrier density of the Au cores upon laser irradiation, which is highly related to the probability of hot electron generation and injection induced by the strong field enhancement of Au NPs and nanoparticles-on-mirror (NPoMs) (Fig. 2b and g). Hot electrons are normally generated with resonance excitation, which experience radiative and non-irradiative decay channels via electron–electron and electron–phonon scattering [34,35]. When a semiconductor (here the Cu$_{2-x}$S) is in contact with Au NP, these hot electrons can enter the conduction band of the semiconductor, which reduces the electron density on the Au. For NPoM, the injected hot electrons can further transport to Au films forming an electric short pass, thereby increasing the gap conductance. Both effects can lead to the shift of plasmons.

The plasmon shift caused by the change in charge density can be analytically calculated as [36]:

$$\Delta\lambda = -\frac{\Delta N}{2N}\lambda_{\mathrm{P}}\sqrt{\varepsilon_\infty + \left(\frac{1}{P} - 1\right)\varepsilon_{\mathrm{d}}}, \quad (1)$$

where ε_{d} is the permittivity of the surrounding dielectric medium, ε_∞ is the background high-frequency permittivity, P is the shape-dependent depolarization factor, λ_{P} is the plasmon wavelength, N is the carrier density and ΔN is the change in carrier density. The carrier density of Au cannot be easily modified by laser irradiation (446 nm) due to its high work function (5.0 eV). However, with

the coating of semiconductor material such as the Cu$_{2-x}$S, hot electron transfer from Au to Cu$_{2-x}$S is possible. This is verified by transient absorption (TA) spectra, where the Au@Cu$_{2-x}$S NPs show two typical modes at 573 and 890 nm, corresponding to the plasmon resonances of Au and Cu$_{2-x}$S, respectively (Fig. 3d and e). The TA of Au@Cu$_{2-x}$S NPs (at 573 nm) presents a lifetime of 0.38 ps, which is approximately six times faster than that of Au NPs (Fig. 3f upper panel and Supplementary Figure S5a and c), suggesting that CT happens from Au to the Cu$_{2-x}$S shells. As the Cu$_{2-x}$S shells receive electrons from Au, their TA spectra decay (at 890 nm) also appears slightly slower than that of the Cu$_{2-x}$S NPs (Fig. 3f lower panel and Supplementary Figure S5b and d). As such, the electron density of Au is reduced due to such CT (Fig. 3g), which results in a positive value of $\Delta\lambda$ as predicted by using Equation (1). Thus, red shift of LSPR is observed when the excitation laser is on, which can shift back due to electron backflow when the laser is switched off (Fig. 2c). With 641-nm laser irradiation, however, no obvious electron dynamics was observed for pure Au NPs (Supplementary Figure S6a) but a clear CT process still happens in the hybrid Au@Cu$_{2-x}$S NPs (Supplementary Figure S6b), indicating that 641-nm light mainly excites the Cu$_{2-x}$S, whose electrons transfer to the Au NP (Supplementary Figs S3c and S6c and d). As such, the electron density of Au NP increases, which results in a slight blue shift (Supplementary Figure S3a) as predicted by using Equation (1).

When Au@Cu$_{2-x}$S NPs are placed on metal films, NPoM constructs are established and a
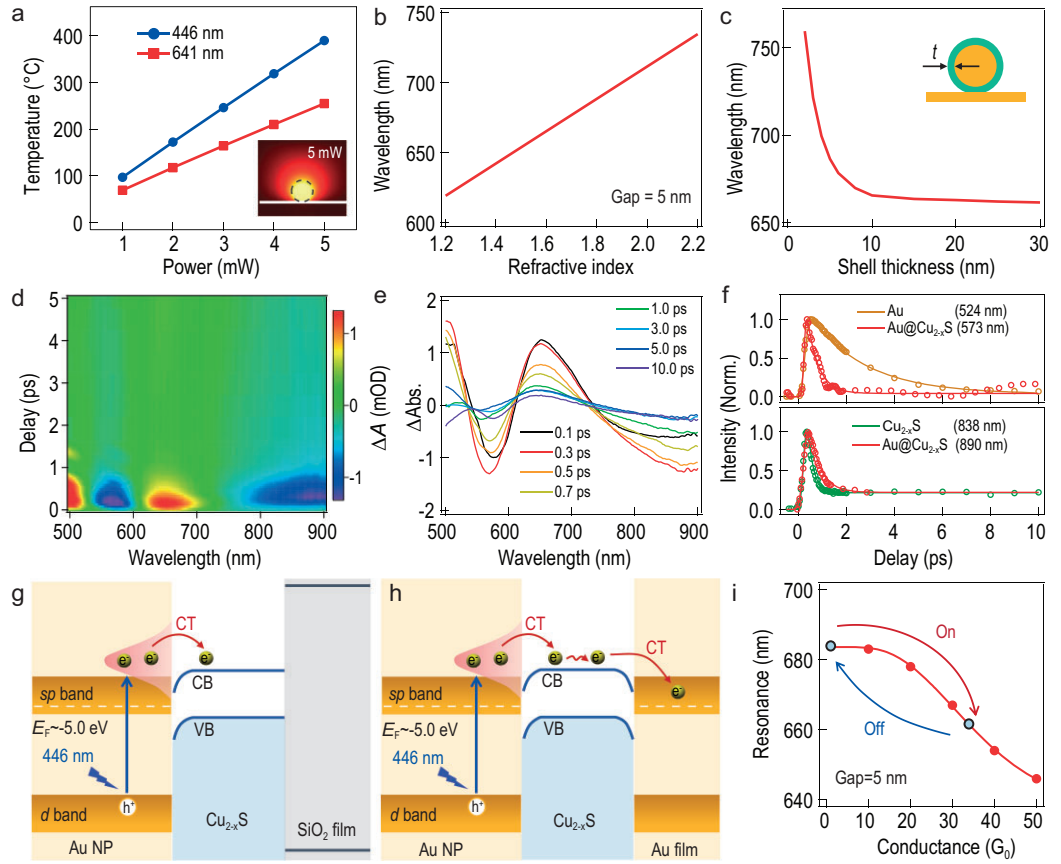
Figure 3. Mechanism investigation of CT in the Au@Cu$_{2-x}$S NPoM system and its influence on the plasmon shift. (a) Temperature calculation of the Au NP irradiated with different laser powers. Inset is the temperature profile around Au with irradiation power of 5 mW. Change in simulated plasmon resonance with (b) RI of the gap medium and (c) the shell thickness. TA spectra of Au@Cu$_{2-x}$S NPs: (d) Kinetic mapping of TA spectra, (e) TA spectra at different probe time, (f) comparison of the electron decay dynamics of Au NP, Au@Cu$_{2-x}$S and Cu$_{2-x}$S, respectively. Schematics of the CT processes in the system of Au@Cu$_{2-x}$S NP on (g) SiO$_2$/Si substrate and (h) Au substrate, respectively. (i) Calculated change in plasmon resonance with gap conductance.

circuit model is applied to qualitatively analyse the antenna mode of this plasmonic system as [16]:

$$\lambda = \lambda_p \sqrt{\varepsilon_\infty + 2\varepsilon_d + 4\varepsilon_d C_g / C_{NP}}, \qquad (2)$$

where C_g and C_{NP} are the capacitance of the structure and NP, respectively. Here we approximate C_g using the formula $C_g = \varepsilon_0 n_g^2 (A/d)$, where A and d are the area of the bottom facet of the Au NP and the gap size, respectively [37]. Since the capacitance is mainly determined by the size of the gap/NP and their dielectric properties, modifying either of these parameters will shift the plasmon resonances (λ). In a certain NPoM structure in which the gap size and dielectric environment are fixed, the gap conductance is critical to the shift in plasmon resonances. The conductance increase contributed from the photothermal effect is small

(0.2G$_0$, Supplementary Figure S7) [38]. Thus, the major contribution to the conductance increase is the hot electron transfer from Au to Cu$_{2-x}$S, which then transports to the Au substrate (Fig. 3h). The conductivity of Cu$_{2-x}$S in the nanogap can be calculated as $\sigma = n \cdot \mu \cdot e$, where n and μ are the charge density and carrier mobility within Cu$_{2-x}$S. e is the unit charge. For 80 nm of Au NPoM with a facet diameter of 10 nm and gap of 5 nm, the calculated gap conductance increase due to hot electron tunneling is ~32G$_0$ (see Methods for the detailed calculation). This large conductance increase can lead to a 18-nm blue shift as predicted by using numerical analysis (Fig. 3i and Supplementary Figure S8), which agrees with the blue shift observed in the experiments (Fig. 2h). Again, with 641-nm laser excitation, because the CT process happens from Cu$_{2-x}$S to Au NPs or Au films (Supplementary Figure S3d), a negligible change in gap conductance is expected, which
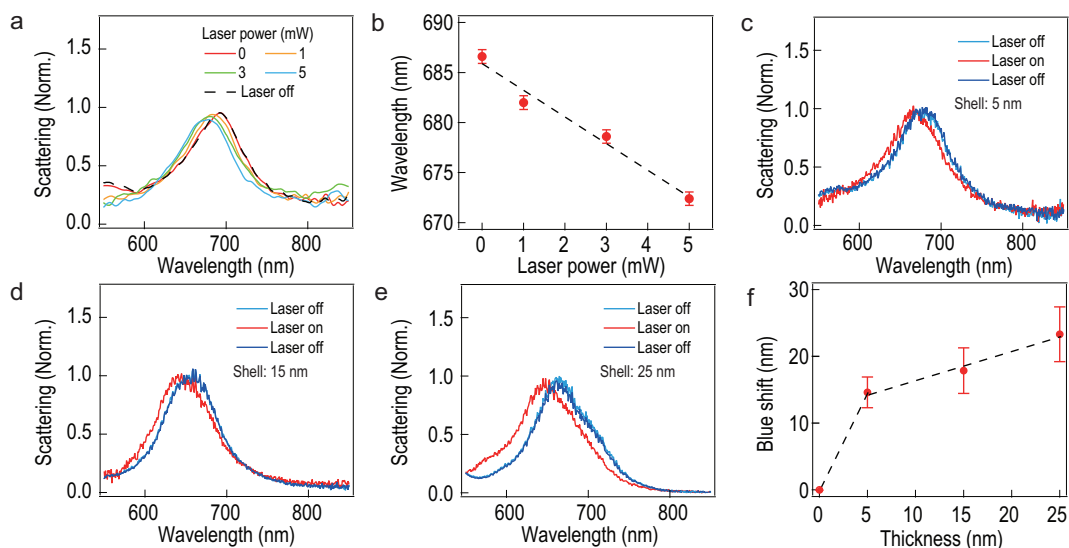
Figure 4. Power- and thickness-dependent plasmon shift of Au@Cu$_{2-x}$S NPoMs. (a) Scattering spectra of Au@Cu$_{2-x}$S NPoM at different irradiation power. (b) Change in plasmon resonance with irradiation power. (c)–(e) Scattering spectra of Au@Cu$_{2-x}$S NPoMs of different shell thickness: (c) 5 nm, (d) 15 nm, (e) 25 nm. Pumping power: 5 mW. (f) Change in blue-shift magnitude with shell thickness. All the error bars are the averaged and squared deviation based on five NPoMs.

reasonably explains no shift in the coupled plasmons (Supplementary Figure S3b).

As the plasmon resonance is determined by the gap conductance, increasing the irradiation power would lead to an increase in the hot carrier concentration (n), which would increase the gap conductance (G). Therefore, we see an increasing blue shift of the gap plasmons with the increase in irradiation power (Fig. 4a and b). The magnitude of the blue shift can also be attenuated with shell thickness. Here, we synthesized Au@Cu$_{2-x}$S NPs of different shell thicknesses by adding different amounts of precursors, which yields uniform shells ranging from 5 to 25 nm (Supplementary Figure S9). As the shell thickness increases, the magnitude of the blue shift increases proportionally at the same pumping power (Fig. 4c–f), which is likely due to the increased carrier mobility of thicker shells [39].

wavelength laser (641 nm) mainly results in excitation of Cu$_{2-x}$S, which induces CT from Cu$_{2-x}$S to Au. As such, we see a slight blue shift of the plasmons due to the increase in the electron density. But this CT does not strongly affect the coupled plasmons in the NPoM geometry as it does not significantly alter the gap conductance. A finite element method (FEM) is applied to simulate the conductance-induced plasmon shift, which agrees well with the experimental results. Unlike the conventional plasmon-tuning strategy, this intriguing tuning mechanism is based on optoelectronic excitation of hot carriers as well as the modification of electron density and gap conductance, which is fast ($\sim$THz) and chip-compatible, meeting the high demands of the ultracompact on-chip integration of functional nanophotonic circuits and photonic computation.

CONCLUSION

In summary, we have demonstrated a dynamic and reversible tuning strategy of plasmon resonances based on optical modulation of hot carrier transport in the semiconductor coating. The hot electrons are generated from interband excitation (446 nm) of Au NP and transfer to the Cu$_{2-x}$S coating, which reduces the electron density of Au, thereby redshifting the LSPR. In the NPoM geometry, such CT enhances the conductance of the plasmonic nanogaps, which results in blue shift of the coupled plasmon resonances. Excitation with a longer-

METHODS

Synthesis of Au@Cu$_{2-x}$S core–shell NPs

The Au@Cu$_{2-x}$S core–shell NPs were synthesized according to a previous report [26]. Specifically, 50 μL of 0.2 M cetyltrimethylammonium bromide (CTAB), 50 μL of 0.1 M hexamethylenetetramine (HMT), 50 μL of 0.1 M AA, 50 μL of 0.01 M TAA and 0.01 M cupric chloride (CuCl$_2$) with varied volume were sequentially added into vials containing 1 mL of Au NP dispersion (Nanopartz), which were incubated at 85°C for 8 h. The hybrid core–shell NPs were harvested by centrifugation at 8000 r/min for

10 min and redispersed in 1 mL of deionized water for stock use.

Characterizations

UV–vis extinction spectra of the Au NPs and hybrid Au@Cu$_{2-x}$S core–shell NPs were collected using an optofiber spectrometer (QE65000, Ocean Optics). The Raman spectra of Cu$_{2-x}$S were obtained using a confocal Raman microscope (Renishaw InVia) equipped with a 532-nm laser. TEM images and energy dispersive EDS were captured at an accelerating voltage of 200 kV (JEOL JEM-F200). Scanning electron microscope (SEM) images were obtained using a Sigma Zeiss at an accelerating voltage of 10 kV. XPS (Thermo Fisher ESCALAB 250Xi) were performed using a monochromatic Al K Alpha (1 486.68 eV) X-ray source under an ultra-high vacuum (10^{-7} mbar). The X-ray high-tension (HT) was 15 kV and the measured spot size was 200 μm.

Optical switching of the plasmon resonances based on Au@Cu$_{2-x}$S NPoM system

To construct the NPoM system, Au@Cu$_{2-x}$S NPs were drop-casted on Au films, which were then placed under a dark-field (DF) microscope (BX53M, Olympus). The scattering spectra of the NPs were recorded confocally through a 100 × DF objective (numerical aperture (NA): 0.8) that were coupled using a 50-μm optical fiber connected to a spectrometer (integration time: 800 ms, QEPro, Ocean Optics). DF scattering spectra were collected simultaneously when an excitation laser (CW) of 446 nm was on. The power of the CW laser was 5 mW and the duration of the laser on/off periods was 1 s each. The PL spectra of the same Au@Cu$_{2-x}$S NPoMs were recorded, which were then used to subtract the scattering spectra to exclude the influence of PL on the shift of plasmons (Supplementary Figure S2). The scattering spectra of Au@Cu$_{2-x}$S NP on SiO$_2$ substrate were measured in the same way as a contrast experiment.

Ultrafast TA spectroscopy

The TA spectra of the Au NPs, Cu$_{2-x}$S NPs and Au@Cu$_{2-x}$S NPs were collected using a commercial TA system (HARPIA, Light Conversion). Specifically, a femtosecond laser (repetition rate of 40 kHz, 1030-nm central wavelength and pulse duration of ~120 fs, PHAROS, Light Conversion) was split into two beams. One beam went through optical parametric amplification (ORPHEUS twins, Light Conversion) to pump the Au@Cu$_{2-x}$S NPs. The other beam went through the delay line, which yields the white light via sapphire as the probe beam. The pump and probe beams were focused on Au@Cu$_{2-x}$S dispersion in a cuvette with wavelengths of 400 and 640 nm. Single exponential fitting $y = y_0 + a_1 \cdot e^{\frac{-(t-t_0)}{\tau}}$ was applied to the TA spectra, which resolves the lifetime of τ.

Simulations

The near-field scattering and temperature profile of Au@Cu$_{2-x}$S NPs on Au film and SiO$_2$ substrate are numerically simulated using FEM. Specifically, a plain wave incidence with energy density equivalent to a Gaussian beam was applied at the Au@Cu$_{2-x}$S NPoMs. The thermal conductivity of Au, Cu$_{2-x}$S and SiO$_2$ are 318, 1.5 and 1.8 W (m·K)$^{-1}$, respectively. The RI of Cu$_{2-x}$S is set at an average value of 1.8 with an imaginary part of 0.02 [40,41]. Gap conductance is calculated based on the formula $G = \sigma \cdot \frac{S}{l}$, where l is the gap size (~5 nm) and S is the area of the bottom facet of the Au NP with a radius of ~5 nm. Conductivity of the gap was calculated based on the formula $\sigma = n \cdot \mu \cdot e$, where n is the carrier density change induced by the hot electron injection, which is ~10^{26} m^{-3}; μ is the carrier mobility of Cu$_2$S, which is estimated to be 0.01 m^2·(V·s)$^{-1}$ [39]; and e is the unit charge (1.6×10^{-19}).

SUPPLEMENTARY DATA

Supplementary data are available at *NSR* online.

AUTHOR CONTRIBUTIONS

T. D. conceived the idea and supervised the project. J. Y., C. Z. and S. M. synthesized the samples, J. Y. performed all the

characterizations. C. W., J. Y. and C. Z. performed TA measurements and data analysis. T. D. and J. Y. performed analytic and numerical calculations. J. Y., T. D., T. W., L. Z., Q. W. and H. X. discussed and analysed the data, wrote and revised the manuscript. All the authors approve the final version of the manuscript.

REFERENCES

1. Brongersma ML and Shalaev VM. The case for plasmonics. *Science* 2010; **328**: 440–1.
2. Jiang N, Zhuo X and Wang J. Active plasmonics: principles, structures, and applications. *Chem Rev* 2018; **118**: 3054–99.
3. Wurtz GA, Pollard R and Hendren W *et al.* Designed ultrafast optical nonlinearity in a plasmonic nanorod metamaterial enhanced by nonlocality. *Nat Nanotechnol* 2011; **6**: 107–11.
4. Wang X, Morea R and Gonzalo J *et al.* Coupling localized plasmonic and photonic modes tailors and boosts ultrafast light modulation by gold nanoparticles. *Nano Lett* 2015; **15**: 2633–9.
5. Rotenberg N, Caspers JN and van Driel HM. Tunable ultrafast control of plasmonic coupling to gold films. *Phys Rev B* 2009; **80**: 245420.
6. Chen F, Wang Y and Wang S *et al.* Plasmon-assisted nanopoling of poly(vinyl difluoride) films. *Adv Opt Mater* 2021; **9**: 2100084.
7. Cormier S, Ding T and Turek V *et al.* Actuating single nano-oscillators with light. *Adv Opt Mater* 2018; **6**: 1701281.
8. Li Q, Chen L and Xu H *et al.* Photothermal modulation of propagating surface plasmons on silver nanowires. *ACS Photonics* 2019; **6**: 2133–40.
9. Kaya S, Weeber JC and Zacharatos F *et al.* Photo-thermal modulation of surface plasmon polariton propagation at telecommunication wavelengths. *Opt Express* 2013; **21**: 22269–84.
10. Wang Y and Ding T. Optical tuning of plasmon-enhanced photoluminescence. *Nanoscale* 2019; **11**: 10589–94.
11. Xing J, Zhao C and Zou Y *et al.* Modulating the optical and electrical properties of $MAPbBr_3$ single crystals via voltage regulation engineering and application in memristors. *Light Sci Appl* 2020; **9**: 111.
12. Michel A-KU, Chigrin DN and Maß TWW *et al.* Using low-loss phase-change materials for mid-infrared antenna resonance tuning. *Nano Lett* 2013; **13**: 3470–5.
13. Rudé M, Simpson RE and Quidant R *et al.* Active control of surface plasmon waveguides with a phase change material. *ACS Photonics* 2015; **2**: 669–74.
14. Seo M, Kyoung J and Park H *et al.* Active Terahertz nanoantennas based on VO_2 phase transition. *Nano Lett* 2010; **10**: 2064–8.
15. Zhang C, Li D and Zhang G *et al.* Switching plasmonic nanogaps between classical and quantum regimes with supramolecular interactions. *Sci Adv* 2022; **8**: eabj9752.
16. Benz F, de Nijs B and Tserkezis C *et al.* Generalized circuit model for coupled plasmonic systems. *Opt Express* 2015; **23**: 33255–69.
17. King PDC and Veal TD. Conductivity in transparent oxide semiconductors. *J Phys: Condens Matt* 2011; **23**: 334214.
18. Qazilbash MM, Brehm M and Chae BG *et al.* Mott transition in VO_2 revealed by infrared spectroscopy and nano-imaging. *Science* 2007; **318**: 1750–3.
19. Rini M, Cavalleri A and Schoenlein RW *et al.* Photoinduced phase transition in VO_2 nanocrystals: ultrafast control of surface-plasmon resonance. *Opt Lett* 2005; **30**: 558–60.
20. Lei DY, Appavoo K and Sonnefraud Y *et al.* Single-particle plasmon resonance spectroscopy of phase transition in vanadium dioxide. *Opt Lett* 2010; **35**: 3988–90.
21. Orlianges JC, Leroy J and Crunteanu A *et al.* Electrical and optical properties of vanadium dioxide containing gold nanoparticles deposited by pulsed laser deposition. *Appl Phys Lett* 2012; **101**: 133102.
22. Boyce AM, Stewart JW and Avila J *et al.* Actively tunable metasurfaces via plasmonic nanogap cavities with Sub-10-nm VO_2 films. *Nano Lett* 2022; **22**: 3525–31.
23. Ma S, Yang DJ and Ding SJ *et al.* Tunable size dependence of quantum plasmon of charged gold nanoparticles. *Phys Rev Lett* 2021; **126**: 173902.
24. Majeski MW, Bolotin IL and Hanley L. Cluster beam deposition of $Cu_{2-x}S$ nanoparticles into organic thin films. *ACS Appl Mater Interfaces* 2014; **6**: 12901–8.
25. Gómez-Solano RE, Arias-Cerón JS and Ríos-Ramírez JJ *et al.* Synthesis and study of structure and phase composition in $Cu_{2-x}S$, Sn_xS_y, ZnS, Cu_xSnS_y and CuZnSnS pellets. *J Mater Sci: Mater El* 2020; **31**: 7519–23.
26. Ma S, Chen K and Qiu YH *et al.* Controlled growth of CdS–$Cu_{2-x}S$ lateral heteroshells on Au nanoparticles with improved photocatalytic activity and photothermal efficiency. *J Mater Chem A* 2019; **7**: 3408–14.
27. Wang S and Ding T. Photothermal-assisted optical stretching of gold nanoparticles. *ACS Nano* 2019; **13**: 32–7.
28. Li G-C, Zhang Y-L and Jiang J *et al.* Metal-substrate-mediated plasmon hybridization in a nanoparticle dimer for photoluminescence line-width shrinking and intensity enhancement. *ACS Nano* 2017; **11**: 3067–80.
29. Zhang Q, Liu D and Ren Q *et al.* Probing electron transport in plasmonic molecular junctions with two-photon luminescence spectroscopy. *Nanophotonics* 2021; **10**: 2467–79.
30. Chen F, Liu Y and Ding T. Fast and hydrosensitive switching of plasmonic nanocavities via photothermal effect. *Photon Res* 2023; **11**: 12–9.
31. Chen F, Yao J and Wang X *et al.* Fast modulation of surface plasmons based on the photothermal effect of nonvolatile solid thin films. *Nanoscale* 2023; **15**: 476–82.
32. Wang S, Guo L and Wen X *et al.* Phase transitions in the Cu_2S nanowires. *Mater Chem Phys* 2002; **75**: 32–8.
33. Liang X, Jin D and Dai F. Phase transition engineering of Cu_2S to widen the temperature window of improved thermoelectric performance. *Adv Electron Mater* 2019; **5**: 1900486.
34. Ho KHW, Shang A and Shi F *et al.* Plasmonic Au/TiO_2-dumbbell-on-film nanocavities for high-efficiency hot-carrier generation and extraction. *Adv Funct Materi* 2018; **28**: 1800383.
35. Peng Z, Lo TW and Lei D. Plasmonic-hot-electron mediated room-temperature generation of charged biexciton in monolayer WS_2. *Phys Rev Materi* 2023; **7**: 054002.

36. Mulvaney P, Pérez-Juste J and Giersig M *et al.* Drastic surface plasmon mode shifts in gold nanorods due to electron charging. *Plasmonics* 2006; **1**: 61–6.

37. Benz F, Tserkezis C and Herrmann LO *et al.* Nanooptics of molecular-shunted plasmonic nanojunctions. *Nano Lett* 2015; **15**: 669–74.

38. Bekenstein Y, Elimelech O and Vinokurov K *et al.* Charge transport in Cu_2S nanocrystals arrays: effects of crystallite size and ligand length. *Z Phys Chem* 2015; **229**: 179–90.

39. Ubale AU, Choudhari DM and Kantale JS *et al.* Synthesis of nanostructured Cu_xS thin films by chemical route at room temperature and investigation of their size dependent physical properties. *J Alloys Compd* 2011; **509**: 9249–54.

40. Zhang J, Xing T and Zhang M *et al.* Facile preparation of $Cu_{2-x}S$ supernanoparticles with an unambiguous SERS enhancement mechanism. *Chem Eng J* 2022; **434**: 134457.

41. Saadeldin M, Soliman HS and Ali HAM *et al.* Optical and electrical characterizations of nanoparticle Cu_2S thin films. *Chin Phys B* 2014; **23**: 046803.